The Astrophysical Journal, 867:81 (11pp), 2018 November 1 https://doi.org/10.3847/1538-4357/aae0f6

The Coronal Volume of Energetic Particles in Solar Flares as Revealed by Microwave Imaging

Gregory D. Fleishman[1], Maria A. Loukitcheva[1,2,3], Varvara Yu. Kopnina[2], Gelu M. Nita[1], and Dale E. Gary[1]
[1] Physics Department, Center for Solar-Terrestrial Research, New Jersey Institute of Technology Newark, NJ 07102-1982, USA
[2] Saint Petersburg Branch of Special Astrophysical Observatory, Pulkovskoye chaussee 65/1, St. Petersburg 196140, Russia
[3] Saint Petersburg State University, 7/9 Universitetskaya nab., St. Petersburg 199034, Russia
Received 2018 August 3; accepted 2018 September 10; published 2018 November 1

Abstract

The spectrum of gyrosynchrotron emission from solar flares generally peaks in the microwave range. Its optically thin, high-frequency component, above the spectral peak, is often used for diagnostics of the nonthermal electrons and the magnetic field in the radio source. Under favorable conditions, its low-frequency counterpart brings additional, complementary information about these parameters as well as thermal plasma diagnostics, either through gyrosynchrotron self-absorption, free–free absorption by the thermal plasma, or the suppression of emission through the so-called Razin effect. However, their effect on the low-frequency spectrum is often masked by spatial nonuniformity. To disentangle the various contributions to low-frequency gyrosynchrotron emission, a combination of spectral and imaging data is needed. To this end, we have investigated Owens Valley Solar Array (OVSA) multi-frequency images for 26 solar bursts observed jointly with *RHESSI* during the first half of 2002. For each, we examined dynamic spectra, time- and frequency-synthesis maps, *RHESSI* images with overlaid OVSA contours, and a few representative single-frequency snapshot OVSA images. We focus on the frequency dependence of microwave source sizes derived from the OVSA images and their effect on the low-frequency microwave spectral slope. We succeed in categorizing 18 analyzed events into several groups. Four events demonstrate clear evidence of being dominated by gyrosynchrotron self-absorption, with an inferred brightness temperature of $\geqslant 10^8$ K. The low-frequency spectra in the remaining events are affected to varying degrees by Razin suppression. We find that many radio sources are rather large at low frequencies, which can have important implications for solar energetic particle production and escape.

Key words: acceleration of particles – Sun: corona – Sun: flares – Sun: radio radiation – Sun: X-rays, gamma rays

1. Introduction

Solar flares produce a variety of transient emissions over the electromagnetic spectrum from radio waves to hard X-rays (HXRs). Nonthermal electrons accelerated in the flares dominate the two ends of the spectrum, microwaves and HXRs. A typical gyrosynchrotron microwave spectrum has a spectral peak frequency at about ~10 GHz flanked by low- and high-frequency slopes that often can be well approximated by power laws (Nita et al. 2004).

Traditionally, the high-frequency, optically thin part of the gyrosynchrotron spectrum has received the greatest attention. Historically, the interest in this high-frequency region developed from the study of supernova remnants and radio galaxies (see, e.g., Ginzburg & Syrovatskii 1965), where the power-law index α of the radio spectrum can be unambiguously related to the power-law index δ of the energy distribution of ultra-relativistic electrons producing synchrotron emission; $\delta = 2\alpha - 1$. Accordingly, a similar interpretation was attempted in early studies of the microwave emission from solar flares. However, it was long ago recognized (e.g., Dulk 1985) that in the solar case the microwave emission is produced by nonrelativistic or only mildly relativistic electrons, for which that simple relationship between the spectral indices no longer holds. Moreover, the gyrosynchrotron spectrum from power-law-distributed nonthermal electrons does not follow a simple power law (Ramaty 1969) but rather the slope decreases with increasing frequency. In addition to the dependence on the energy spectrum, the gyrosynchrotron spectral slope varies strongly in the presence of any pitch-angle anisotropy of the nonthermal electrons (Fleishman & Melnikov 2003). Therefore, the energy spectrum of radiating electrons cannot reliably be derived from the radio slope alone. Instead, either a forward fit (Gary et al. 2013) or realistic 3D modeling (Nita et al. 2015) is needed to extract plasma and particle diagnostics from microwave emission.

With 3D modeling (see, e.g., Fleishman et al. 2016b, 2016c; Kuroda et al. 2018), however, the strong diagnostic potential of the low-frequency part of the microwave spectrum becomes apparent. Such modeling helps to recover the spatial distributions of nonthermal electrons and magnetic field (and, in some cases, of the thermal plasma) in addition to the energy distribution of nonthermal electrons. In particular, the modeling vividly reveals the theoretically expected link between the microwave emission spectral shape at the low frequencies and the source area, which may be strongly frequency dependent (Bastian et al. 1998; Kuznetsov et al. 2011). This suggests that having simultaneous information about the microwave spectrum and associated source area from imaging at various frequencies would allow a more accurate interpretation of the radio spectrum and the realization of its diagnostic potential.

Imaging of the low-frequency part of the microwave spectrum is needed for reliable diagnostics because, in addition to its area dependence, a few other effects can shape it: gyrosynchrotron self-absorption (Dulk 1985) by the nonthermal electrons themselves, the suppression of the emission via the Razin effect (Melnikov et al. 2008), and free–free absorption by the thermal plasma (Bastian et al. 2007). The latter two effects require a dense plasma, with free–free absorption requiring in addition a relatively low temperature.

Although in the case of a uniform source all these cases could be distinguished by studying the microwave spectral shape alone, the commonly occurring source nonuniformity complicates the interpretation greatly; thus, considering the spectral and spatial data together is needed to disentangle the different factors forming the microwave spectrum at low frequencies. The paucity of such spectral imaging explains the relative lack of attention that has been given to the spectrum below the peak frequency.

Surprisingly, there have been only a few isolated studies of gyrosynchrotron source sizes or locations relative to other flare-associated sources at frequencies $f \lesssim 5$ GHz. Kucera et al. (1993) and Willson (1993) reported observations with the Very Large Array at 327 MHz and 1.4 GHz, which yielded a conclusion that there can be multiple microwave sources at low frequencies, with much larger total source area than is typical at higher frequencies. In their review paper, Bastian et al. (1998) used a combination of a few observations and simple models to conclude that "typically, the characteristic source scale declines roughly as f^{-1}"; however, this should only be considered a general qualitative trend, from which individual cases can deviate substantially. There has been little progress on these ideas since then, likely because of the many studies based on the solar-dedicated Nobeyama Radioheliograph (NoRH) (Nakajima et al. 1994), which operates at high, optically thin frequencies (17 and 34 GHz) and drew attention to diagnostics at those frequencies. But even at the frequencies of NoRH or at the lower frequency (5.7 GHz) of the Siberian Solar Radio Telescope (Grechnev et al. 2003), we are aware of no statistical study on source area even though the data needed for that are available.

Another solar-dedicated instrument, the Owens Valley Solar Array (OVSA; Gary & Hurford 1994) provided interferometry data suitable for imaging since 2000; however, until recently only a very few solar bursts have been imaged (see, e.g., Lee & Gary 2000; Nita et al. 2005; Fleishman et al. 2011, 2016c) because of the challenge of calibrating the OVSA data. Recently, however, a calibrated OVSA database and corresponding analysis tools have been produced (Nita et al. 2014) enabling us and others to perform more studies of the microwave source areas and locations at various frequencies in a broad spectral range, ~1–15 GHz. In this paper we consider a subset of solar bursts observed simultaneously with OVSA and *RHESSI* (Lin et al. 2002) during the first four months of the *RHESSI* operation. Our subset includes one M-class and 15 C-class flares; we specifically did not include any strong flares, which typically involve extreme spatial complexity. For all of these events we obtain the dependence of source area on frequency and classify the events into various groups according to which physical effects are responsible for forming the low-frequency part of the spectrum. We give a few examples of these distinctly behaving events and discuss the implications of our findings for understanding solar flares.

2. OVSA Instrument: Microwave Spectroscopy and Imaging

At the time of observations, the OVSA interferometer consisted of six antennas of different diameters: two large antennas with a diameter of 27 m and four small ones with a diameter of 1.8 m. Observations were carried out at 40 characteristic frequencies in the frequency range 1–18 GHz. The study required supplementing observations in the X-ray domain to verify the correct positioning of the interferometric images. Therefore, initially the criterion for the selection of events was the presence of observational data simultaneously in the OVSA and *RHESSI* databases. A list of solar flares observed simultaneously by the OVSA and *RHESSI* instruments was compiled, and contains events from 2002 February 15 (the start date of *RHESSI* observations) to 2002 July 1.

Here we specifically concentrate on microwave imaging, along with spectral radio data obtained with OVSA. The spectral data consist of the total power data from OVSA at 40 frequencies spaced roughly logarithmically from 1 to 18 GHz. In particular, the peak frequency of the bursts falls within the OVSA spectral range during the burst, so the spectral shape of the microwave emission, which includes the spectral peak along with low- and high- frequency slopes, is well captured by OVSA alone.

The OVSA imaging capability and the adopted calibration scheme described at its Web site (see also Fleishman et al. 2016a for a brief description) provide imaging of solar flares at many adjacent frequencies between around 1 and 15 GHz, which is a significant advance compared with other radio instruments available during solar cycle 23. Unfortunately, there are also disadvantages of OVSA imaging, the most severe of which is a relatively small number of baselines available, thus greatly undersampling the *uv* points needed for robust imaging. The relatively low sensitivity of the OVSA array for calibration, combined with the complex instrumental configuration, also makes reliable imaging a significant challenge, and the quality of imaging varies from event to event. For this reason, in this paper we rely on only the zeroth-order imaging property—that of the source area—but as a check on quality we do require that source locations agree with independently observed positions from *RHESSI* as described below.

3. Event Selection and Analysis

In the period from 2002 February 15 to July 1 there are 55 events recorded by OVSA.[4] Of these, 37 are accompanied by observations with *RHESSI*. For the analysis of the microwave source areas performed here, there is no explicit use of the *RHESSI* data aside from our use of the *RHESSI* source locations to check the validity of the OVSA imaging: the ability of the OVSA data to reproduce the correct source location (verified using direct comparison with *RHESSI* images; see Figure 1) is an important initial check on the validity of the OVSA phase calibration for a given event. From the sample of these 37 OVSA events, about half are unsuitable for calibration and analysis due to incompleteness, low quality, or high noise. There remain 23 bursts for which the OVSA imaging was possible. Since in some cases there are several sub-bursts in the dynamic spectrum, which are treated in this study as separate events, the total number of events increases to 26. Of these 26 events, only those with data for at least two frequencies below the peak frequency are selected to analyze the low-frequency part of the spectrum, which yields the final list of 18 events listed in Table 1. For each of these events we applied the algorithm described in the OVSA Imaging Manual[5] to create images at as many frequencies as possible using the

[4] The initial OVSA observation files in the ARC format are freely available at http://ovsa.njit.edu/data/archive.

[5] http://ovsa.njit.edu/legacy/Manual4OVSA_imaging_2017.pdf

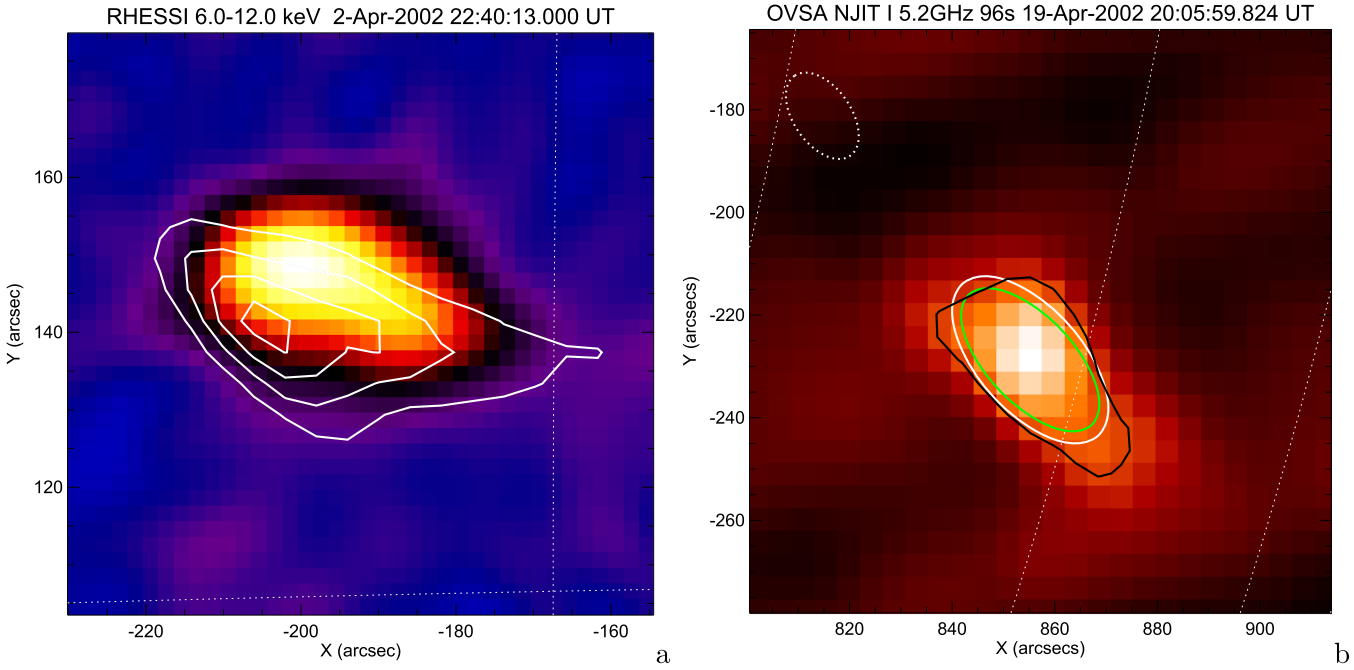

Figure 1. (a) Example of the spatial relationship between an HXR source obtained by *RHESSI* at 6–12 keV (background image) and a microwave OVSA image obtained by time (72 s) and frequency (3.2–7.4 GHz) synthesis using the CLEAN+SelfCal method (white contours at 30%, 50%, 70%, and 90%). (b) Illustration of OVSA image and its derived quantities: 96 s synthesis OVSA image at 5.2 GHz (red background) with 50% intensity contour (black line); Gaussian model of the OVSA beam (white dotted oval); Gaussian fit to the OVSA image (white solid oval); deconvolved Gaussian source (green solid oval).

Table 1
List of Events

#	*GOES*	Event	Pos	NOAA	t_{start}	t_{peak}	F_{peak}, sfu	f_{peak}, GHz
1	C7.6	20020328_1755	N08W62	9881	17:55:31	17:57:27	23	6.6
2	C2.3	20020402_2240	N01E12	9887	22:40:05	22:40:29	30	5.1
3	C1.7	20020408_1842	N18E15	9899	18:43:02	18:43:26	27	6.7
4	C2	20020408_1847	N18E15	9899	18:41:18	18:47:30	32	6.4
5	C6.1	20020408_2038	N18E15	9899	20:40:12	20:44:04	20	6
6	M4.0	20020412_1756	N21W25	9901	17:43:01	17:56:09	98	4.3
7	M4.0	20020412_1744	N21W25	9901	17:44:17	17:45:18	87	6.2
8	C?	20020413_1935	N21W37	9893	19:31:48	19:35:08	12	6
9	C2.0	20020414_1940	S04E35	9907	19:40:27	19:41:19	33	5.4
10	C4.4	20020414_2054	S03E34	9907	20:50:58	20:54:18	21/20	4.9/ 2.0
11	C4.4	20020414_2055	S03E34	9907	20:55:06	20:55:18	16	4.2
12	C1	20020418_2251	S15W39	9906	22:51:17	22:52:25	14	5.7
13	C1.6	20020419_2004	S13W67	9906	20:04:19	20:06:39	24	5.6
14	C3.9	20020503_1804	S17E49	9934	18:04:47	18:05:39	20	4.9
15	C3.2	20020503_2333	S17E49	9934	23:32:51	23:33:35	345	12.1
16	C2.7	20020504_2145	S17E37	9934	21:43:05	21:45:49	31	6.9
17	C2.4	20020522_2050	S23E37	9961	20:50:15	20:51:11	14	4
18	C2.5	20020529_1746	S16E62	9973	17:46:24	17:47:04	50	9

time synthesis technique over the duration of the event peak, and saved them in FITS format for further analysis.

These images were used to determine the measured sources areas (biased by the frequency-dependent beam size) as well as "deconvolved" source areas, where the effect of the finite beam has been removed. The measured areas were straightforwardly computed by accounting for the source area within the 50% contour. To obtain the deconvolved areas we employed an analytical deconvolution method proposed by Wild (1970), which requires that both the beam and the true source be well approximated by 2D Gaussian distributions; see Figure 1(b) for the illustration. In this case, the observed source brightness is another Gaussian, from which the true source Gaussian can be determined exactly given that the beam shape is known. In our study we fit the brightness distributions for all events and at all frequencies of interest with the corresponding Gaussians, and then deconvolved the beam to determine the "true" source whose area could straightforwardly be found as the ellipse area πab, where a and b are the semimajor and semiminor axes of the ellipse. Even though the Gaussian fit to the source brightness distribution is not perfect in many cases, as illustrated by Figure 1(b), the source area is well reproduced as illustrated by Figure 2: the regression between the area of the fitted Gaussian (S_f) and the measured (within the 50% contour)

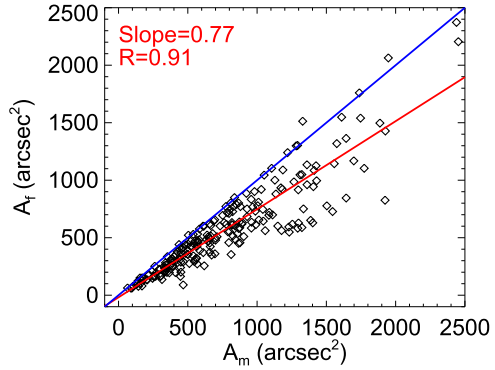

Figure 2. Scatter plot showing the areas of the Gaussian fitted model vs. area measured within the 50% brightness contour. The blue line shows an ideal $y = x$ correspondence, while the red line shows the cross-correlation established using the presented data, which demonstrates that the fit systematically underestimates the area, but this is typically within 25%, according to the regression law $A_f \propto A_m$.

area (S_m), $S_f = 0.77 S_m$ is highly statistically significant (the correlation coefficient is $R = 0.91$); this tell us that the Gaussian fit systematically underestimates the source area by 25% on average, which is acceptable for our study.

The source areas obtained this way are then fit for each event using power laws quantified by the area extrapolated to 1 GHz and the corresponding power-law index. Although we do not have the area measurements at the reference frequency of 1 GHz, it is convenient to use this value uniformly for all events.

4. Classification of the Events

4.1. Radio Brightness, Spectra, and Sizes: Theoretical Foundation

The radio flux density F_σ of a given polarization σ (=−1 or 1 for the extraordinary [X] or ordinary [O] modes, respectively) can be computed by integrating the brightness temperature, T_b, of the source over the solid angle $d\Omega$ (Dulk 1985; Fleishman & Toptygin 2013):

$$F_\sigma = \frac{n_\sigma^2 f^2}{c^2|\cos\theta|} k_B \int T_b d\Omega \approx \frac{f^2}{c^2} k_B \times \int T_b d\Omega \quad [\mathrm{erg\ cm^{-2}\ s^{-1}\ Hz^{-1}}], \tag{1}$$

where n_σ is the index of refraction of a given mode, $|\cos\theta| = \frac{c}{v_g}|\frac{\partial(\omega n_\sigma)}{\partial\omega}|^{-1}$, θ is the angle between the wave vector and the group velocity $\boldsymbol{v}_g$ vector, k_B is the Boltzmann constant, and c is the speed of light; the second (approximate) definition (Dulk 1985) is valid when $n_\sigma \approx 1$ and $|\cos\theta| \approx 1$, i.e., at frequencies large compared with the plasma resonance frequencies. Evaluating the integral using the mean value theorem we obtain the radio flux density F_I expressed in solar flux units (sfu) (Fleishman et al. 2016b)

$$F_I = F_{\mathrm{LCP}} + F_{\mathrm{RCP}} \simeq 12\ [\mathrm{sfu}] \left(\frac{f}{1\ \mathrm{GHz}}\right)^2 \times \left(\frac{T_b}{10^7\ \mathrm{K}}\right)\left(\frac{A}{10^{20}\ \mathrm{cm^2}}\right); \tag{2}$$

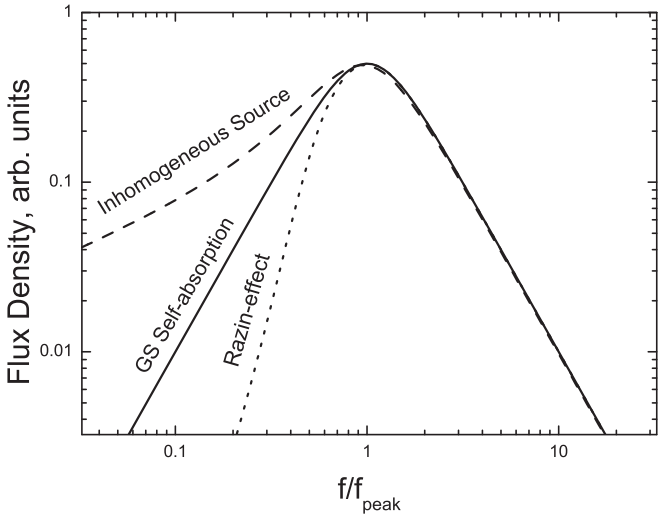

Figure 3. Schematic representation of the microwave spectral shape by the Razin effect, gyrosynchrotron self-absorption, and source nonuniformity.

where $T_b = T_b(f)$ is a peak brightness temperature of the source at the frequency f and $A = A(f)$ is an effective source area at this frequency at the level of half maximum (this estimate becomes exact for a Gaussian distribution of the source brightness temperature on the sky). Note that both the brightness temperature and the source area depend on frequency in the general case.

For a source of constant area and uniform brightness temperature, Equation (2) implies that the flux density F_I increases as f^2. However, actual flare spectra deviate from this expectation due to several effects shown schematically in Figure 3. The largest effect is varying optical depth, which starts out high (is optically thick) at lower frequencies, then becomes unity near the peak of the spectrum (the turn-over frequency), and then falls below unity (becomes optically thin) at still higher frequencies. In the optically thick regime, $T_b \approx T_{\mathrm{eff}}$ (Dulk 1985), where T_{eff} is the effective temperature defined by the source function S_σ: $k_B T_{\mathrm{eff}} \approx c^2 S_\sigma / f^2$. For example, for the plasma described by a Maxwellian distribution, T_{eff} is equivalent to the plasma temperature T. For the gyrosynchrotron emission produced by nonthermal electrons, however, the effective temperature is much higher than the plasma temperature. Given that the plasma temperature is high during flares, usually well above 10 MK, we expect still higher nonthermal brightness temperatures $T_{\mathrm{eff}} \gg 10^7$ K. Typically, $T_{\mathrm{eff}} \sim 10^8$–$10^9$ K in solar radio bursts, although it may be even higher in strong events. When the optical depth τ falls below unity (in the optically thin part of the spectrum), however, the brightness temperature becomes $T_b \approx \tau T_{\mathrm{eff}}$. Other effects that cause deviations from a simple f^2 spectrum are that (1) T_{eff} is a function of frequency for a non-Maxwellian distribution of emitting particles, generally rising with frequency due to the fact that higher-energy particles are more effective at radiating at higher frequencies, (2) the Razin effect can modify (suppress) the low-frequency part of the spectrum if the plasma is reasonably dense, (3) the free–free absorption may play a role if the plasma is both dense and cool, and (4) due to source inhomogeneity the area of the source is a function of frequency, as already mentioned.

Table 2
Event Classification

#	f_{peak}	f_{range}		LF Spectral	Area at 1 GHz			Power Index			Case	Case
	GHz	GHz	GHz	Index	Beam	Source	Dsource	Beam	Source	Dsource	Spatial	Spectral
1	6.6	2.6	8.6	0.97	6727	25932	15369	−2.00	−2.18	−2.27	C	R
2	5.1	3.2	7.4	3.23	4069	3044	928	−2.00	−1.21	−0.83	C	R
3	6.7	2.4	7.8	0.87	4677	7390	2826	−2.18	−1.87	−1.62	C	S
4	6.4	3.4	7.8	0.92	4781	9311	8227	−2.21	−1.74	−2.01	C	(R)
5	6	3.4	8.6	1.10	3195	3155	670	−2.00	−1.17	−0.58	C	R
6	4.3	2.8	5.6	5.44	3728	8759	764595	−2.12	−2.19	−6.10	C	S
7	6.2	2.8	6.6	1.73	2090	3266	1516	−1.58	−1.10	−0.87	C	S-(R)
8	6	3.4	5.4	1.10	3190	10851	7436	−2.00	−1.98	−2.00	C	R
9	5.4	3.4	7.0	2.02	3171	2415	1223	−2.00	−0.91	−0.66	C	(S)-R
10	4.9/ 2.0	3.8	7.4	1.58	3206	3835	2247	−2.00	−1.38	−1.34	C	R
11	4.2	2.6	4.8	2.70	3205	2746	815	−2.00	−1.06	−0.56	C	R
12	5.7	3.8	6.2	2.30	5679	87502	144338	−2.00	−2.76	−3.42	C	R
13	5.6	6.2	7.8	4.30	4452	22904	20095	−2.23	−2.23	−2.30	(U)	R
14	4.9	3.2	7.4	3.43	6070	23597	10799	−2.00	−2.20	−2.20	(U)	R
15	12.1	5.6	14.0	2.45	7644	12573	8394	−2.09	−2.00	−2.2	C	S
16	6.9	4.8	7.4	2.98	3435	1391	92	−2.00	−1.07	0.03	U	(S)
17	4	2.6	5.0	3.53	4147	5359	2409	−2.13	−1.36	−1.03	(U)	R
18	9	6.2	14.0	2.45	2572	62510	179087	−2.00	−2.90	−3.62	C	S-R

To distinguish between the cases dominated by either self-absorption or the Razin effect, we consider frequency dependences of all factors entering Equation (2). Recall that, in the optically thick regime (i.e., when the self-absorption dominates), the brightness temperature follows a power law $T_b \propto f^{\beta_{lf}}$ with the index $\beta_{lf} \sim 0.5$–0.9 for a power-law distribution of nonthermal electrons, or $\beta_{lf} = 0$ for the thermal case (Dulk 1985). Thus, in a uniform source (i.e., the area does not depend on frequency), the flux density will follow a power law $F_I \propto f^{\alpha_{lf}}$ with $\alpha_{lf} = \beta_{lf} + 2 \sim 2.5$–$2.9$. The spectrum can be flatter (see Figure 3) if the area increases toward lower frequencies. In contrast, within the Razin effect, the brightness temperature falls quickly toward lower frequencies, thus much larger values of the spectral indices, $\beta_{lf} > 0.9$ and $\alpha_{lf} > 2.9$, are expected (Figure 3). However, if the source is nonuniform, so that the source area falls with frequency as $A \propto f^{\gamma}$ (γ is negative) the observed spectral index will become $\alpha_{lf} = \beta_{lf} + 2 + \gamma$ and, thus can become reasonably small even under the Razin effect. Here the observational information about the frequency dependence of the source area can be employed to solve for a "corrected" spectral index $\alpha_{lf_{corr}}$ of the source as it would be observed if it had the same area at all frequencies, $\alpha_{lf_{corr}} = \beta_{lf} + 2 = \alpha_{lf} - \gamma$ and make a classification based on this, "corrected" spectral index.

Equation (2) can be solved for the brightness temperature

$$T_b \approx 1.56 \times 10^{10}[\mathrm{K}] \frac{F_I\ [\mathrm{sfu}]}{f^2_{[\mathrm{GHz}]} A} \tag{3}$$

where the area A is measured in arcsec^2 or, alternatively, for the area:

$$A \approx 156 \frac{F_I\ [\mathrm{sfu}]}{f^2_{[\mathrm{GHz}]}} \left(\frac{10^8\ \mathrm{K}}{T_b} \right). \tag{4}$$

Having just two measurements at a given frequency—the flux density and the source area—allows the brightness temperature to be computed using Equation (3). If these are known at many frequencies, the obtained values allow the brightness temperature spectrum to be deduced and, based on that, each frequency range can be roughly categorized as optically thick or thin. Note that the brightness temperature of the optically thick emission is equivalent to the effective temperature (energy) of the electrons producing this emission. In solar flares, the energy of nonthermal electrons is typically above 10 keV, which implies that the expected brightness temperature is above 10^8 K; we will use this value as a demarcation between the optically thin and potentially optically thick regimes.

It is important to realize that it is not at all easy to reliably distinguish between the optically thin and thick cases at frequencies below the spectral peak. Indeed, the spectral turnover of the gyrosynchrotron emission can be due to either gyrosynchrotron self-absorption (the low-frequency emission is optically thick in this case) or suppression of the gyrosynchrotron emissivity and absorption coefficient (when the refractive index falls below unity because of high plasma density, the so-called Razin effect; see, e.g., Ramaty 1969). In this case the source remains optically thin even below the spectral peak frequency and never becomes thick at the low-frequency range because the gyrosynchrotron absorption coefficient decreases almost exponentially toward lower frequencies. A combination of the two effects is also possible: the spectral peak and its immediate vicinity can be controlled by gyrosynchrotron self-absorption, while the Razin effect can step in at lower frequencies and result in a progressively steeper low-frequency slope.

The shapes of the gyrosynchrotron spectrum in a uniform source vividly differ in the two cases (see Figure 3 and examples of the computed spectra in, e.g., Fleishman & Melnikov 2003). The gyrosynchrotron self-absorption results in a quasi-power-law, low-frequency slope with a "local" spectral index slowly rising from zero (at the spectral peak) to values smaller than 3 at lower frequencies; spectral oscillations around small integer multiples of the gyrofrequency may be present at the lowest frequencies. In contrast, the Razin effect produces a spectrum that falls more rapidly (almost exponentially; see the dotted line in Figure 3) toward lower frequencies. In practice, even though radio bursts with a reasonably steep low-frequency slope exist (Fleishman et al. 2016a), in many

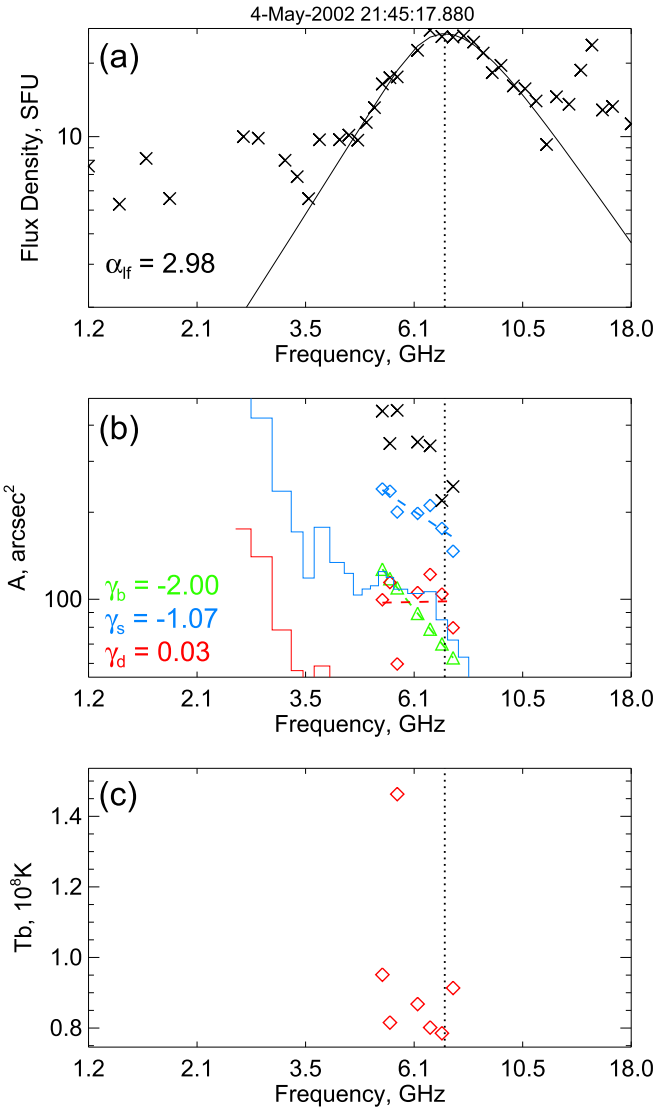

Figure 4. Uniform source example with a steep low-frequency slope and almost flat dependence of the source area on frequency. Top: total power microwave spectrum (crosses) obtained with OVSA and spectral fit with the generic function (solid line). Middle: dependence of areas on the frequency: area measured within 50% contour of the synthesized image (blue crosses); area of the Gaussian ellipse fitted to the brightness distribution (blue diamonds); area of the OVSA array beam (green triangles); area obtained from the Gaussian deconvolved model source (red diamonds). The areas of the beam, as well as of the fitted and deconvolved sources are computed as πab, where a and b are the corresponding semimajor and semiminor ellipse axes. Dashed blue, red, and green lines show the corresponding power-law fits to the data. Red histograms show the "expected" area of the source computed at each frequency for the given observed radio flux using Equation (4) assuming that the brightness temperature at the spectral peak frequency is $T_b = 10^8$ K (upper histogram) or $T_b = 3 \times 10^8$ K (lower histogram) and the frequency dependence $T_b \propto f^{-0.8}$. Bottom: dependence of the mean brightness temperature on frequency.

cases when there are independent signatures of the Razin effect, e.g., from the spectral peak frequency constancy in time, the spectra remain much flatter than expected for the Razin effect (Melnikov et al. 2008). The likely reason for this is well understood: it is due to a spatial non-uniformity of the radio source. In terms of Equation (2) this non-uniformity may be described as an increase of the source area toward lower frequencies, which is the only way of compensating for the drop in T_b toward lower frequencies. Ideally, a combination of the spectral and imaging data can help to separate the frequency dependence of the brightness temperature from that of the source area and, thus to classify the source as being thin or thick, which is needed to interpret the diagnostics based on the microwave total power data. The physically different cases in our classification are the dominance of either effect, gyrosynchrotron self-absorption or the Razin effect, or a combination of both in either (quasi-)uniform or nonuniform source; thus, six different meaningful classes of sources are logically possible plus, perhaps, a seventh class of unclassifiable cases, e.g., in the case of spatially unresolved sources.

4.2. Categorization of the Events

Here we will categorize the events according to the properties they demonstrate, separately, in the spatial and spectral domains. If the source area (after the beam deconvolution) does not depend on frequency, we will classify the event as being uniform and mark it with the letter U; otherwise, the source is spatially complex and marked C. In the spectral domain, we categorize the events according to the process responsible for forming the low-frequency slope of the spectrum (to the left from the spectral peak); we distinguish cases dominated by self-absorption (S) or the Razin effect (R). In the case of some ambiguity in assigning a given property, we put the corresponding attribute in parentheses. For example, the combination of attributes U in the spatial domain and S in the spectral domain implies that in the given event we have a spatially uniform radio source, whose low-frequency slope is formed by gyrosynchrotron self-absorption, while the attribute (S) tells that dominance of the self-absorption in forming the low-frequency part of the radio spectrum is more likely than the Razin effect; attributes S-R mean that we have clear indications of both self-absorption and the Razin effect in the given event, while the designations (S)-R/S-(R) mean that the presence of gyrosynchrotron self-absorption/the Razin effect is ambiguous but likely.

Table 2 lists the results of the classification for all 18 events. It gives the spectral peak frequency, the spectral range employed for the area analysis, the low-frequency spectral indices, and the fit parameters (area at 1 GHz and the area spectral index γ) for the beam, observed source, and deconvolved source. The last two columns show the event attributes according to the adopted classification nomenclature. Below we describe a number of events representative of all identified event types.

4.3. Examples

4.3.1. Example of a Uniform Source: SOL20020504T2145

Uniform sources are, prehaps not surprisingly, very rare in our data set. Figure 4 shows the spectrum and the frequency dependence of the beam and source areas for the weak microwave burst of solar event SOL20020504T2145. Only frequencies near the spectral peak are bright enough for reliable analysis. The area of the deconvolved source does not show any dependence on frequency (dashed red line in Figure 4(b)), which is consistent with expectations for a uniform source. The low-frequency spectral slope, $\alpha_{lf} \approx 2.98$, is slightly steeper than the value of 2.9 expected for the optically thick spectrum; however, we are inclined to classify this case as an optically thick uniform source given that a uniform source with the Razin effect would show a progressive steepening toward the

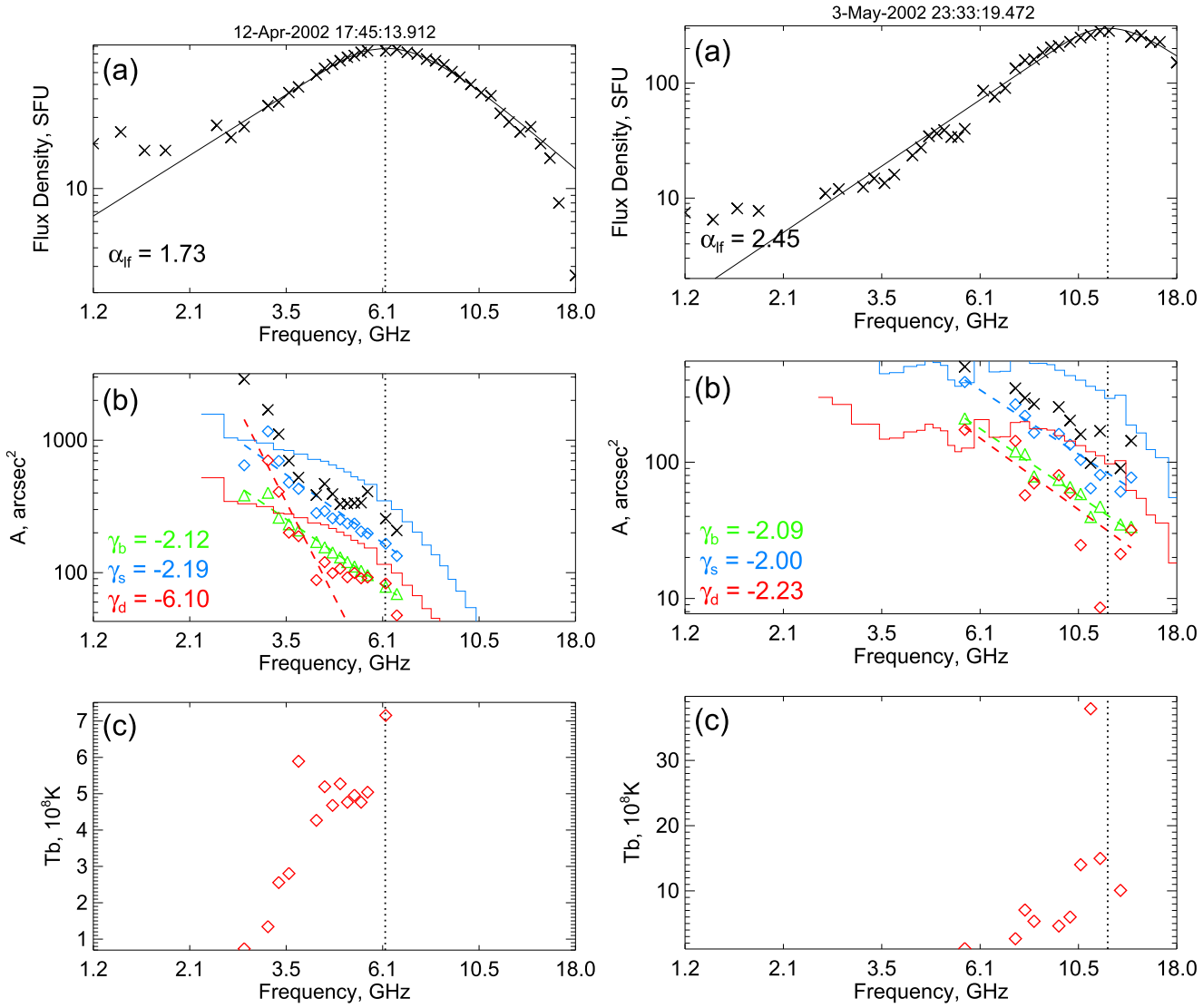

Figure 5. Examples of optically thick, spatially nonuniform sources. The figure layout is the same as in Figure 4.

lower frequencies, which is not observed. In addition, the brightness temperature at the spectral peak frequency is about 10^8 K, which is consistent with the self-absorption effect. We note, however, that this consideration pertains to only the main spectral peak around 6 GHz. We cannot rule out that another spectral component is present at lower frequencies, where the signal is too low for our quantitative analysis.

4.3.2. Nonuniform Optically Thick Sources

Examples of sources where the effect of the gyrosynchrotron self-absorption is combined with nonuniformity of the source are given in Figure 5; these are the events SOL20020412T1745 and SOL20020503T2333. In both cases the brightness temperature is high, $T_b \gtrsim 3 \times 10^8$ K, while the spectral slopes are shallower than expected for a uniform source. This is consistent with the area rising toward the lower frequency as observed.

4.3.3. Nonuniform Sources with Steep Spectra and Razin Effect Signature

Examples of sources where the Razin effect is combined with nonuniformity of the source are given in Figure 6; these are the events SOL20020419T2006 and SOL20020522T2050. In these cases the low-frequency spectral slopes are remarkably steep, $\alpha_{lf} = 4.3$ and 3.53, respectively; however, the deconvolved source areas still grow toward lower frequencies, which is an indication of source nonuniformity. This is, however, not surprising, given that even events with reasonably steep low-frequency spectra were found to show a significant spatial complexity (Fleishman et al. 2016a). Here both spectral steepness and low brightness temperatures (large source areas) are consistent with the Razin effect playing the dominant role at low frequencies.

4.3.4. Nonuniform Sources with Shallow Spectra and Razin Effect Signature

Figure 7 shows an example (SOL20020413T1935) of a source with a shallow low-frequency spectrum, which might be misinterpreted as gyrosynchrotron self-absorption, but whose brightness temperature is low ($\sim 10^7$ K), which is more consistent with the Razin effect. Note that in a comprehensive study based on the entire 2001–2002 OVSA database, many events with quite shallow low-frequency spectra were,

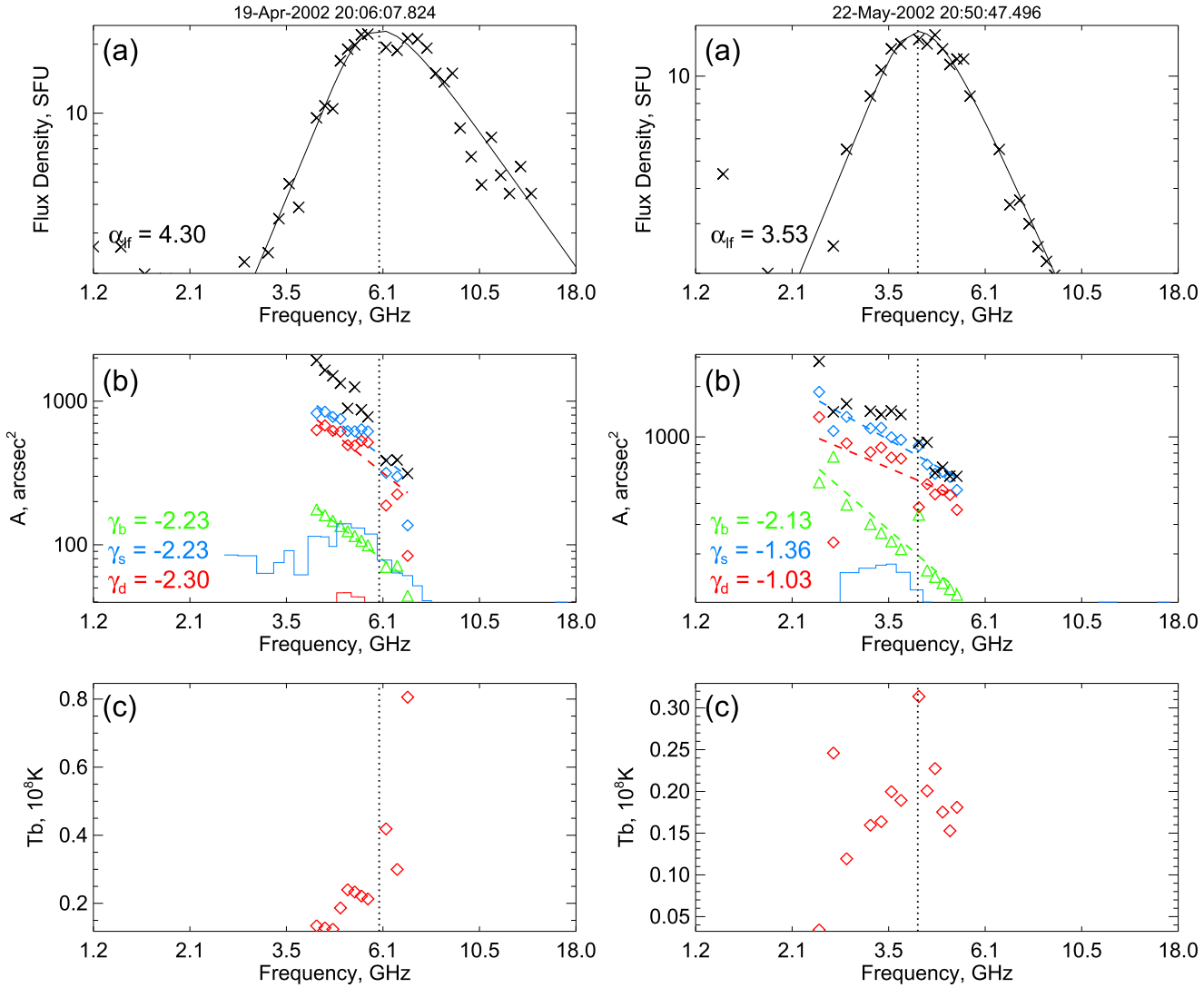

Figure 6. Examples of large sources with a low brightness temperature—a signature of Razin effect dominance, which is also consistent with reasonably large, low-frequency spectral indices of 4.3 or 3.5. The figure layout is the same as in Figure 4.

nevertheless, found to show signatures of the Razin effect based on their temporal evolution (Melnikov et al. 2008).

4.3.5. Nonuniform Sources with Varying Spectral Slope, Self-absorption, and Razin Effect Signature

An example of a case in which the gyrosynchrotron self-absorption and Razin-effect are combined with nonuniformity of the source is given in Figure 8; this is the event SOL20020529T1746. In such cases, the low-frequency spectral slope shows a progressive steepening toward lower frequencies starting from $\alpha_{lf} = 2.45$. The deconvolved source area grows toward lower frequencies, which is an indication of source nonuniformity. The brightness temperature drops significantly toward lower frequencies, which confirms the interpretation of a combination of all possible effects in these events: non-uniformity, gyrosynchrotron self-absorption, and the Razin effect.

5. Statistics

Having the information about the spectral slope, the radio flux density, and the source areas at different frequencies, we categorize all events in Table 1 according to the adopted classification approach, which is indicated in the last column of Table 2. We plot the histogram of the area spectral index occurrence in Figure 9, where we present the areas of both the Gaussian fit and the deconvolved source along with the corresponding value for the array beam. These histograms are important because it is not automatically guaranteed that OVSA imaging yields genuine source areas given the relatively small number of baselines. Nevertheless, Figure 9 shows that the frequency dependence of the beam area on the frequency follows the expected $1/f^2$ dependence, while the source areas, both Gauss-fitted and deconvolved, show a significant scatter of values from 0 to -4, which confirms that the measured source areas are dominated by the actual source area rather than by the array beam.

Figure 10(a) shows two histograms of the source areas at the spectral peak frequency: the expected computed one based on the radio flux density and an assumed "typical" brightness temperature ($T_b = 10^8$ K), and the measured one based on the imaging and image deconvolution. An interesting finding is that the measured areas after deconvolution are typically larger than the expected ones. This is further confirmed by

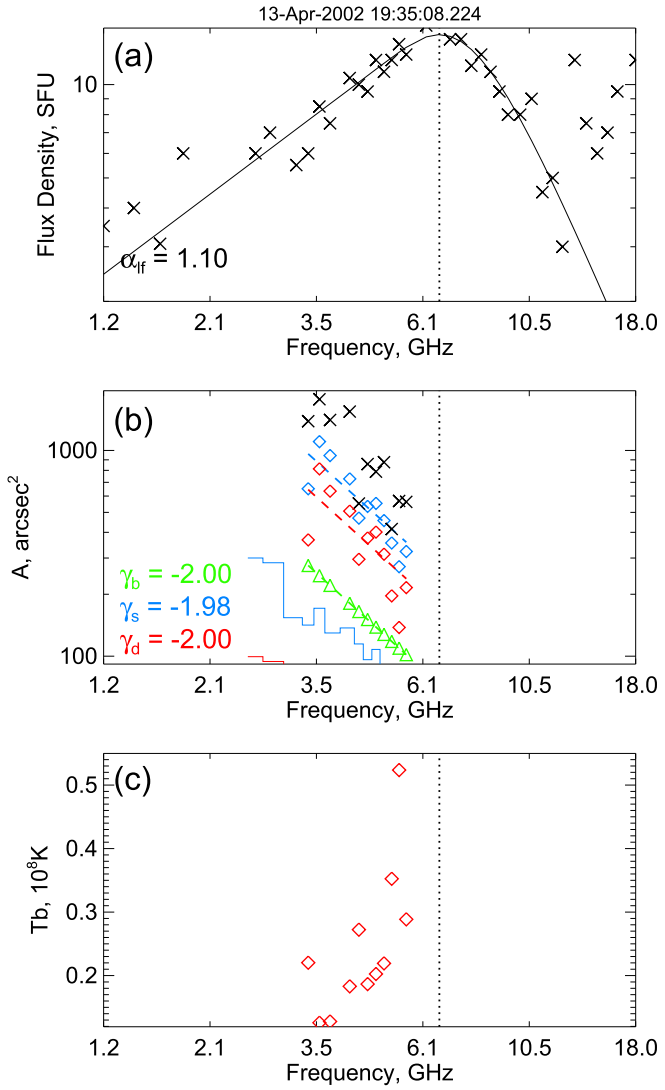

Figure 7. Example of a similarly large source with a low brightness temperature as in Figure 6—a signature of Razin effect dominance, but in this case with a relatively shallow low-frequency spectrum described by index 1.1. This is a clear indication of the spatial nonuniformity of the source, which is further confirmed by the rapid increase of the source area toward lower frequencies. The figure layout is the same as in Figure 4.

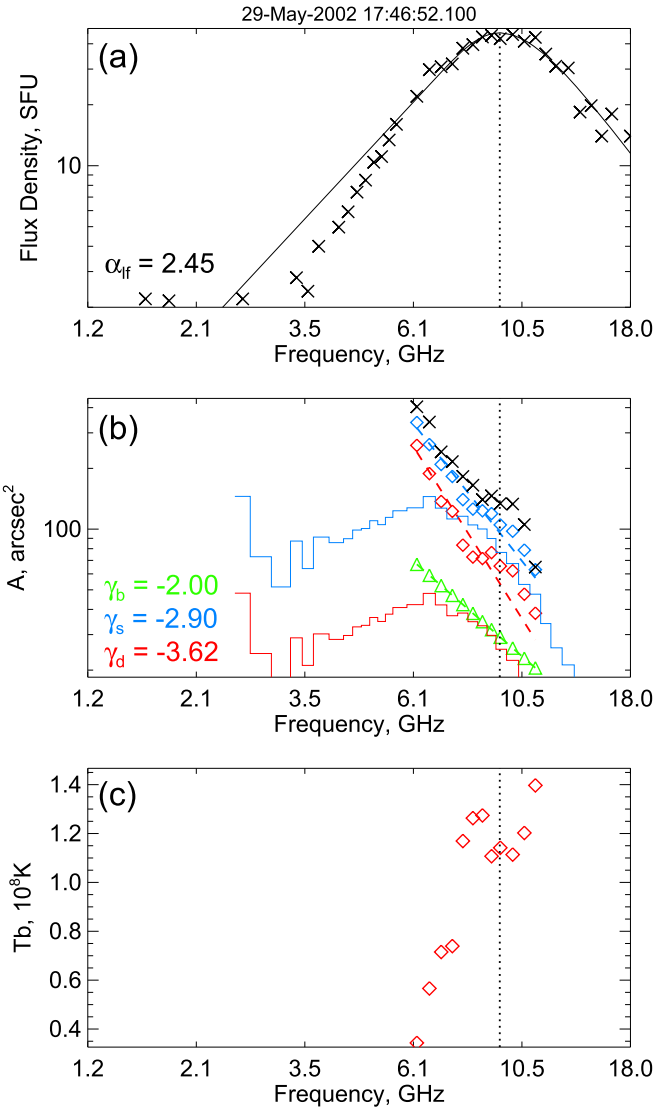

Figure 8. Event showing a combination of all effects: self-absorption, Razin effect, and spatial nonuniformity, which is vividly illustrated by the fact that the brightness temperature is high around the spectral peak but then drops very quickly toward lower frequencies. The figure layout is the same as in Figure 4.

Figure 10(b), where the measured areas are plotted versus the expected ones; the black solid line shows the $y = x$ diagonal. This line can be used to split our events onto two groups: (i) the events below the line have a smaller areas than expected based on the observed flux density and reasonably modest assumption about the brightness temperature. Given that their areas are smaller than expected, we conclude that their brightness temperatures are higher than the $T_b = 10^8$ K adopted to plot the diagonal line; thus, these are the optically thick cases. In contrast, (ii) the events above the diagonal line show low brightness temperature and large areas. These events are likely optically thin cases, where the spectral peak is formed due to the Razin effect.

Figure 11(a) shows the brightness temperature T_b versus peak flux $F_{\rm peak}$ at the spectral peak frequency. It shows that these two quantities are correlated but not linearly proportional to each other: $T_b \propto F_{\rm peak}^{1.55}$ (or $F_{\rm peak} \propto T_b^{0.65}$). This implies that the peak flux density of events increases slower than the brightness temperature, which suggests that sources with higher

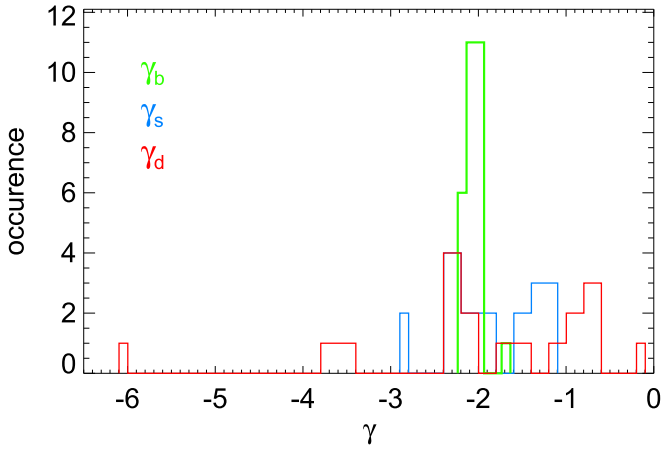

Figure 9. Occurrence rate of the area spectral indices γ for the measured (blue) and deconvolved (red) sources and the OVSA beam (green) for 18 events with a well presented low-frequency part of the OVSA spectra. Deconvolution was performed assuming Gaussian shapes for source and beam using analytical formulae derived by Wild (1970).

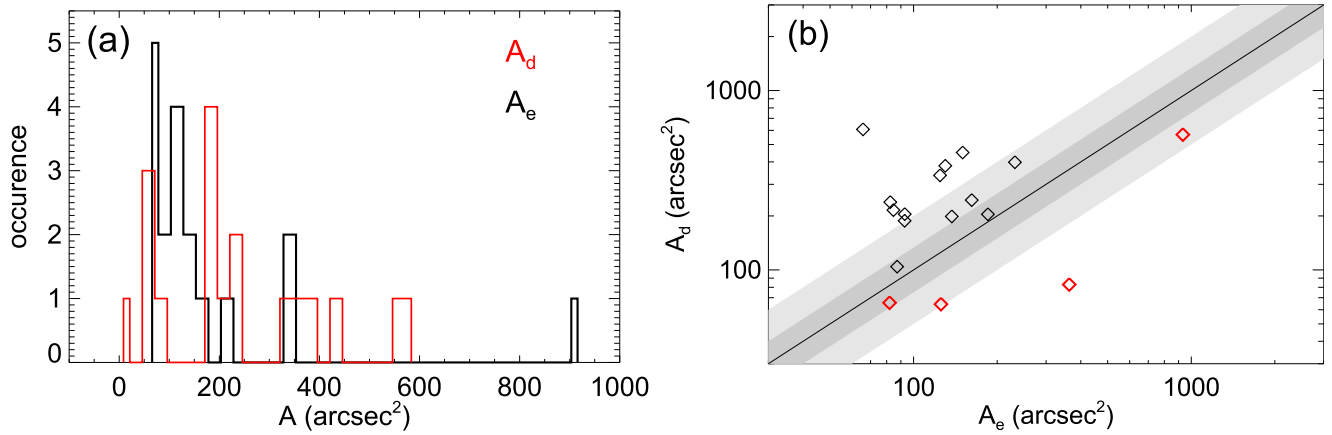

Figure 10. Comparison of the measured and estimated source area. (a) Histograms of the deconvolved source areas (red) and estimated areas assuming brightness temperature $T_b = 10^8$ K (black) at the spectral peak frequency. (b) Scatter plot of the deconvolved and estimated source areas. The black line denotes $A_d = A_e$, while the gray shades show 25% and 50% deviations from that line. Events which lie below this line are plotted in red.

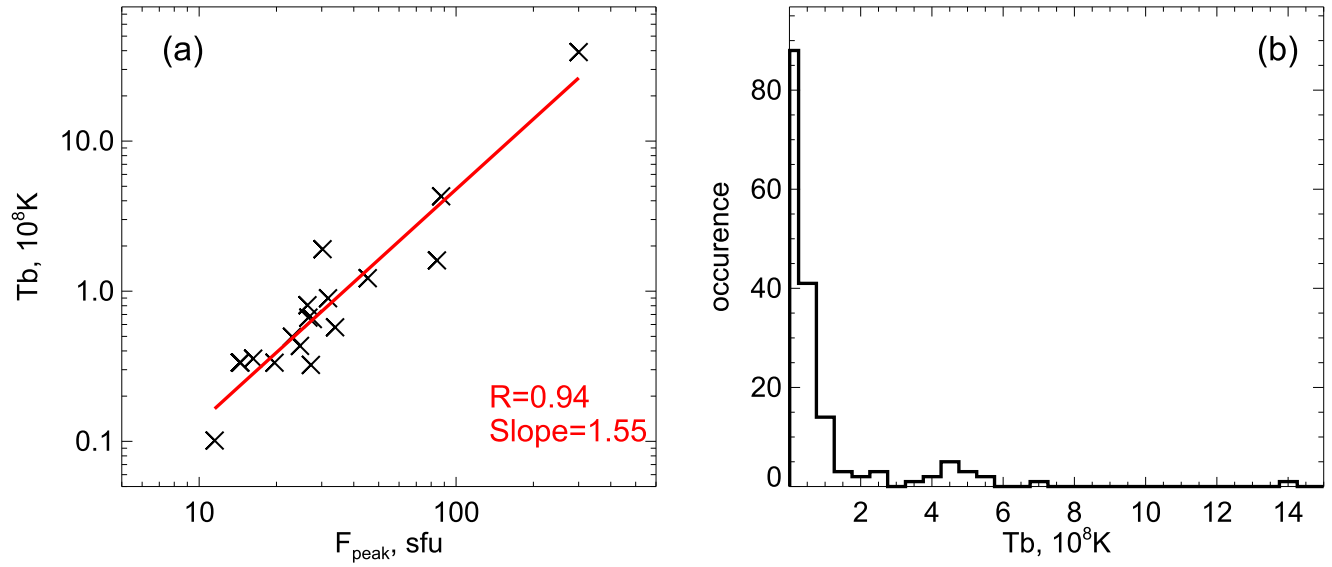

Figure 11. (a) Scatter plot T_b vs. flux density at the spectral peak frequency. (b) Occurrence of the brightness temperature at all frequencies and all events considered. In the majority of cases the brightness temperature is below 10^8 K.

brightness temperature preferentially tend to have lower areas. Figure 11(b) shows the histogram of all brightness temperatures measured at all frequencies at and below the spectral peak. It shows that the majority of the events/frequency points show a brightness temperature below 10^8 K, suggesting that most of them are optically thin due to the Razin effect.

6. Discussion and Conclusions

In this study we have created and made available a partial database of OVSA microwave imaging data for 18 flares jointly observed with *RHESSI*. In the given study, the use of *RHESSI* data was very limited—just to double check and validate the overall locations of the OVSA images. However, the imaging data can be used in future studies employing combinations of microwave and X-ray data.

This paper concentrates on such properties of the microwave data themselves as the frequency-dependent areas and brightness temperatures of the microwave sources. We found that in most cases the microwave sources are resolved with OVSA, so meaningful and valuable information about the source areas can be obtained from the data. Moreover, in most cases, the effect of the frequency-dependent beam size of the array can be removed from the data using the analytical source deconvolution following Wild (1970), which allows us to firmly derive the brightness temperature and area separately. Comparing with a typical brightness temperature, $T_b = 10^8$ K, allows us to classify the sources as to whether they are suppressed by the Razin effect or not, while the frequency dependence of the area allows us to quantify their spatial nonuniformity. Typically, the source area increases toward lower frequency as $A \propto f^{\gamma}$ with a negative γ between -0.5 and -3.5 in agreement with a "typical" value of -2 reported by Bastian et al. (1998) but with a significant scatter. Unfortunately, we do not have sufficient statistics to firmly quantify the distribution of the γ indices. Most (all but one) of the sources clearly show a signature of spatial nonuniformity.

It is interesting to discuss the frequency dependence of the brightness temperature. As we mentioned in Section 4.2, the brightness temperature from a uniform source decreases toward lower frequency compared with that at the spectral peak frequency. In the data we analyzed, however, such a decrease takes place in only slightly more than half of all events (10 of 18).

The rate of this decrease is observed to vary strongly from one event to another: in some cases the slope is very shallow, while in others the brightness temperature falls abruptly below a certain frequency (which is an indication of the Razin effect due to dense plasma). Four events show no trend of the brightness temperature with frequency, or show a large scatter of the data points, which makes it difficult to reveal any trend. Four remaining events show the brightness temperature rising toward the lower frequencies. This trend might be explained as involving large sources of weaker magnetic field, where more energetic electrons contribute to the radio brightness (e.g., Kuroda et al. 2018).

Perhaps, surprisingly, only a minority (five) of the bursts show a behavior consistent with the dominance of gyrosynchrotron self-absorption and, even for some of those, a contribution from the Razin effect is likely. To some extent, this might be an outcome of our selected set of events, which does not include particularly strong bursts, in which the self-absorption typically dominates over the Razin effect. The majority of the bursts in our set show relatively large areas and low brightness temperatures more easily consistent with the optically thin emission due to the Razin effect. This tells us that the thermal plasma density in the microwave sources is relatively high in most of the flares in our sample.

The finding that the areas of the radio sources at low frequencies (weak magnetic field) are rather large can have substantial implications for solar energetic particle production. Indeed, these relatively large low-frequency radio sources may contain a significant number of nonthermal electrons, whose microwave emission is, however, weak due to the Razin effect in a source with weak magnetic field, but a reasonably dense plasma. We note that large low-frequency radio sources have been reported, e.g., by Fleishman et al. (2017) and Kuroda et al. (2018), although in those cases the radio brightness was high, likely because of a lack of the Razin effect (due to a more tenuous plasma). This implies that having large radio sources at low frequency can be common, whether the plasma density is small or large. This means that the nonthermal electrons accelerated in solar flares occupy a much larger volume that can be traced by high-frequency microwave or X-ray imaging.

This work was supported in part by NSF grant AGS-1817277 and NASA grants NNX16AL67G, 80NSSC18K0015, 80NSSC18K0667, and 80NSSC18K1128 to the New Jersey Institute of Technology and RFBR grant 16-02-00749.

ORCID iDs

Gregory D. Fleishman https://orcid.org/0000-0001-5557-2100
Maria A. Loukitcheva https://orcid.org/0000-0001-5246-9044
Gelu M. Nita https://orcid.org/0000-0003-2846-2453
Dale E. Gary https://orcid.org/0000-0003-2520-8396

References

Bastian, T. S., Benz, A. O., & Gary, D. E. 1998, ARA&A, 36, 131
Bastian, T. S., Fleishman, G. D., & Gary, D. E. 2007, ApJ, 666, 1256
Dulk, G. A. 1985, ARA&A, 23, 169
Fleishman, G. D., Kontar, E. P., Nita, G. M., & Gary, D. E. 2011, ApJL, 731, L19
Fleishman, G. D., & Melnikov, V. F. 2003, ApJ, 587, 823
Fleishman, G. D., Nita, G. M., & Gary, D. E. 2017, ApJ, 845, 135
Fleishman, G. D., Nita, G. M., Kontar, E. P., & Gary, D. E. 2016a, ApJ, 826, 38
Fleishman, G. D., Pal'shin, V. D., Meshalkina, N., et al. 2016b, ApJ, 822, 71
Fleishman, G. D., & Toptygin, I. N. 2013, Cosmic Electrodynamics, Astrophysics Space Science Library, Vol. 388 (New York: Springer)
Fleishman, G. D., Xu, Y., Nita, G. N., & Gary, D. E. 2016c, ApJ, 816, 62
Gary, D. E., Fleishman, G. D., & Nita, G. M. 2013, SoPh, 288, 549
Gary, D. E., & Hurford, G. J. 1994, ApJ, 420, 903
Ginzburg, V. L., & Syrovatskii, S. I. 1965, ARA&A, 3, 297
Grechnev, V. V., Lesovoi, S. V., Smolkov, G. Y., et al. 2003, SoPh, 216, 239
Kucera, T. A., Dulk, G. A., Kiplinger, A. L., et al. 1993, ApJ, 412, 853
Kuroda, N., Gary, D. E., Wang, H., et al. 2018, ApJ, 852, 32
Kuznetsov, A. A., Nita, G. M., & Fleishman, G. D. 2011, ApJ, 742, 87
Lee, J., & Gary, D. E. 2000, ApJ, 543, 457
Lin, R. P., Dennis, B. R., Hurford, G. J., et al. 2002, SoPh, 210, 3
Melnikov, V. F., Gary, D. E., & Nita, G. M. 2008, SoPh, 253, 43
Nakajima, H., Nishio, M., Enome, S., et al. 1994, IEEEP, 82, 705
Nita, G. M., Fleishman, G. D., & Gary, D. E. 2014, AAS Meeting, 224, 218.45
Nita, G. M., Fleishman, G. D., Kuznetsov, A. A., Kontar, E. P., & Gary, D. E. 2015, ApJ, 799, 236
Nita, G. M., Gary, D. E., & Fleishman, G. D. 2005, ApJL, 629, L65
Nita, G. M., Gary, D. E., & Lee, J. 2004, ApJ, 605, 528
Ramaty, R. 1969, ApJ, 158, 753
Wild, J. P. 1970, AuJPh, 23, 113
Willson, R. F. 1993, ApJ, 413, 798